Supporting Information

Optimization of electrochemically synthesized $Cu_3(BTC)_2$ by Taguchi method for CO_2/N_2 separation and data validation through artificial neural network (ANN) modeling

Kasra Pirzadeh, Ali Asghar Ghoreyshi*, Mostafa Rahimnejad, Maedeh Mohammadi
Chemical Engineering Department, Babol Noshirvani University of Technology, Babol, Iran
Tel: +98-(11)-32334204, Fax: +98-(11)-32334501
*Corresponding Email: aa_ghoreyshi@nit.ac.ir

1. IAST methodology

Ideal Adsorbed Solution Theory (IAST) is based on the data that is obtained from adsorption isotherms of pure gases to find the selectivity of their mixture [1, 2]. To find out the relation between the two equilibrium phases, Raoult`s law (in vapor/liquid equilibrium) based on the following equation can be used:

$$Py_i = P_i = x_i P_i^0(\pi), \qquad i = 1, 2, 3, ..., N \tag{S1}$$

where y_i and x_i are the mole fractions of component i in the gas phase and adsorbed phase, respectively, and $P_i^0(\pi)$ is the pressure of component i at the same spreading pressure as that of the mixture. The spreading pressure (π) could be given by the following equation:

$$\pi = \frac{(R_g T)}{A}\int_0^{P_1^0}\frac{q_1}{P_1}dP_1 = \frac{(R_g T)}{A}\int_0^{P_2^0}\frac{q_2}{P_2}dP_2 = ... = \frac{(R_g T)}{A}\int_0^{P_N^0}\frac{q_N}{P_N}dP_N \tag{S2}$$

where A is the specific surface area of the adsorbent ($m^2.kg^{-1}$), R_g is the gas constant (J/mol.K), T is the temperature (K), and q is the amount adsorbed ($mmol.g^{-1}$) at total pressure of P (MPa). Hence, the reduced spreading pressure of the sorbed phase, z, can be calculated by:

$$z = \frac{A\pi}{R_g T} = \int_0^{P_1^0(\pi)} \frac{q_1}{P_1} dP_1 = \int_0^{P_2^0(\pi)} \frac{q_2}{P_2} dP_2 = ... = \int_0^{P_N^0(\pi)} \frac{q_N}{P_N} dP_N \quad \text{(S3)}$$

As mentioned before, the adsorption equilibrium data of pure CO_2 and N_2 on opt-$Cu_3(BTC)_2$ were well-described by Langmuir isotherm model. Therefore, combining the Langmuir model with the IAST (Eq. S3), lead to determination of *z* which can be given by the following equation:

$$z_i = q_{\max,i} \ln(1 + b_i P_i^0(\pi)) \quad \text{(S4)}$$

Since at the equilibrium state, the reduced spreading pressures is considered equal for each component, therefore:

$$z_1 = z_2 \quad \text{(S5)}$$

where subscripts 1 and 2 denotes CO_2 and N_2, respectively. Combination of Eqs. (S1), (S4) and, (S5), result in:

$$q_{\max,CO_2} \ln(1 + \frac{b_{CO_2} P y_{CO_2}}{x_{CO_2}}) - q_{\max,N_2} \ln(1 + \frac{b_{N_2} P y_{N_2}}{x_{N_2}}) = 0 \quad \text{(S6)}$$

where ($q_{\max,CO_2}, b_{CO_2}$) and ($q_{\max,N_2}, b_{N_2}$) are Langmuir fitting constants for pure CO_2 and N_2, respectively. At given P and y, the unknown parameter (x) in the Eq. (S6) could be determined. Finally, the adsorption selectivity (S_{CO_2/N_2}) could be calculated through the following equation:

$$S_{CO_2/N_2} = \frac{x_{CO_2} y_{N_2}}{x_{N_2} y_{CO_2}} \quad \text{(S7)}$$

2. Adsorption isotherm study

In the analysis of adsorption processes, adsorption isotherm models can provide information into possible interactions between adsorbent surface and adsorbate molecules which helps better to

interpret the experimental observations [3]. As it was mentioned earlier, to determine CO_2/N_2 selectivity through IAST method, single gas adsorption must be carried out. To this end, all 16 synthesized samples were exposed to mentioned gases and the adsorption capacity of all samples at 298 K as well as their Langmuir curve fitting are illustrated in Fig. S1.

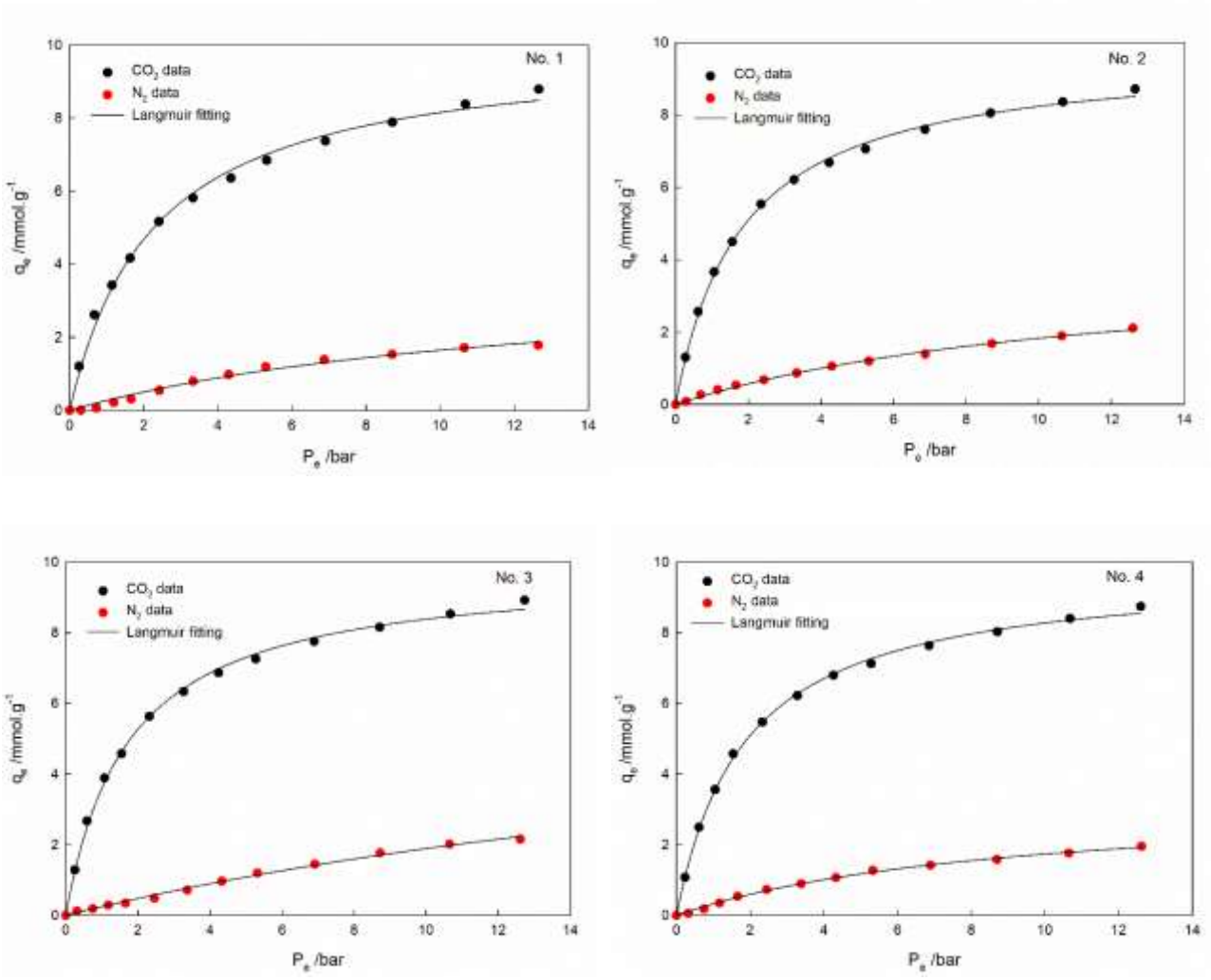

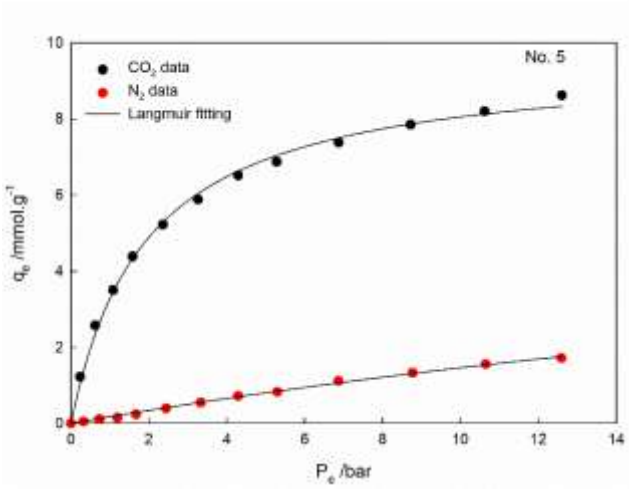
No. 5
CO2 data
N2 data
Langmuir fitting
qe /mmol.g-1
Pe /bar

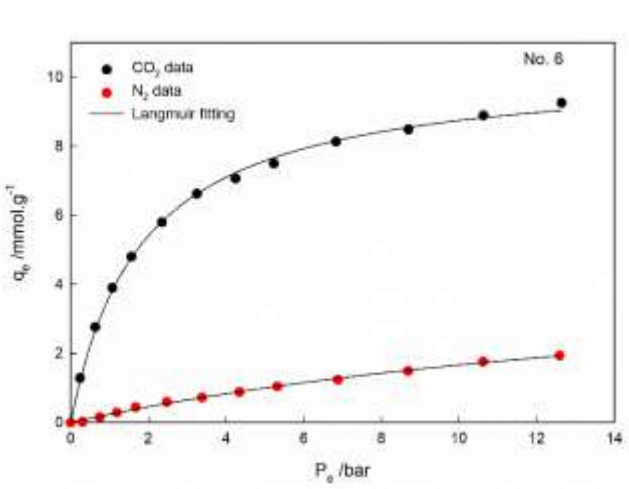
No. 6
CO2 data
N2 data
Langmuir fitting
qe /mmol.g-1
Pe /bar

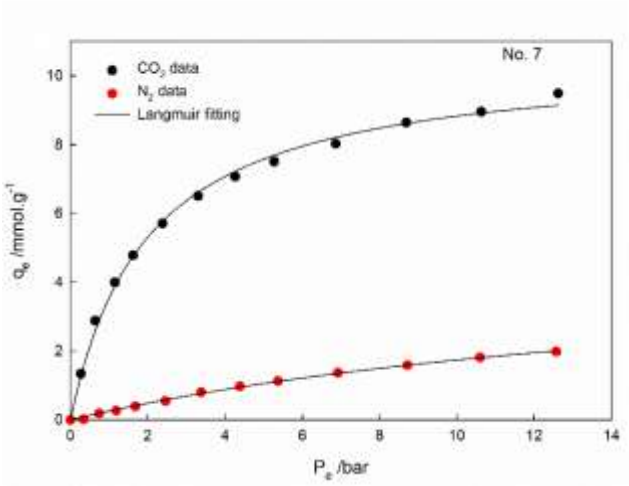
No. 7
CO2 data
N2 data
Langmuir fitting
qe /mmol.g-1
Pe /bar

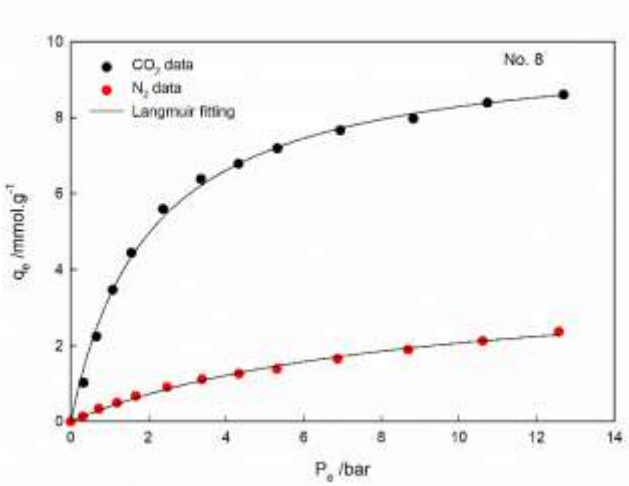
No. 8
CO2 data
N2 data
Langmuir fitting
qe /mmol.g-1
Pe /bar

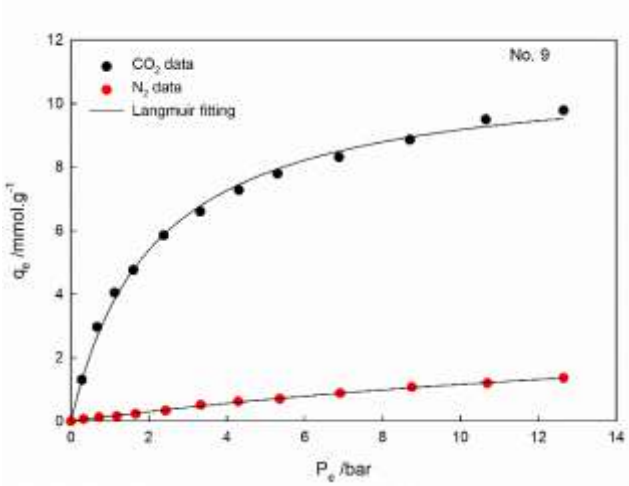
No. 9
CO2 data
N2 data
Langmuir fitting
qe /mmol.g-1
Pe /bar

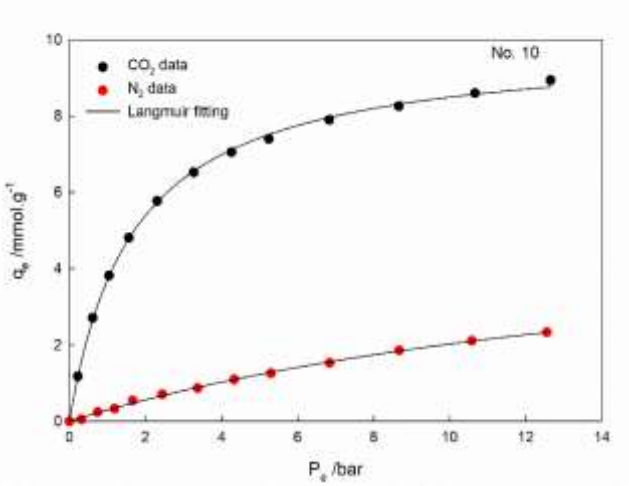
No. 10
CO2 data
N2 data
Langmuir fitting
qe /mmol.g-1
Pe /bar

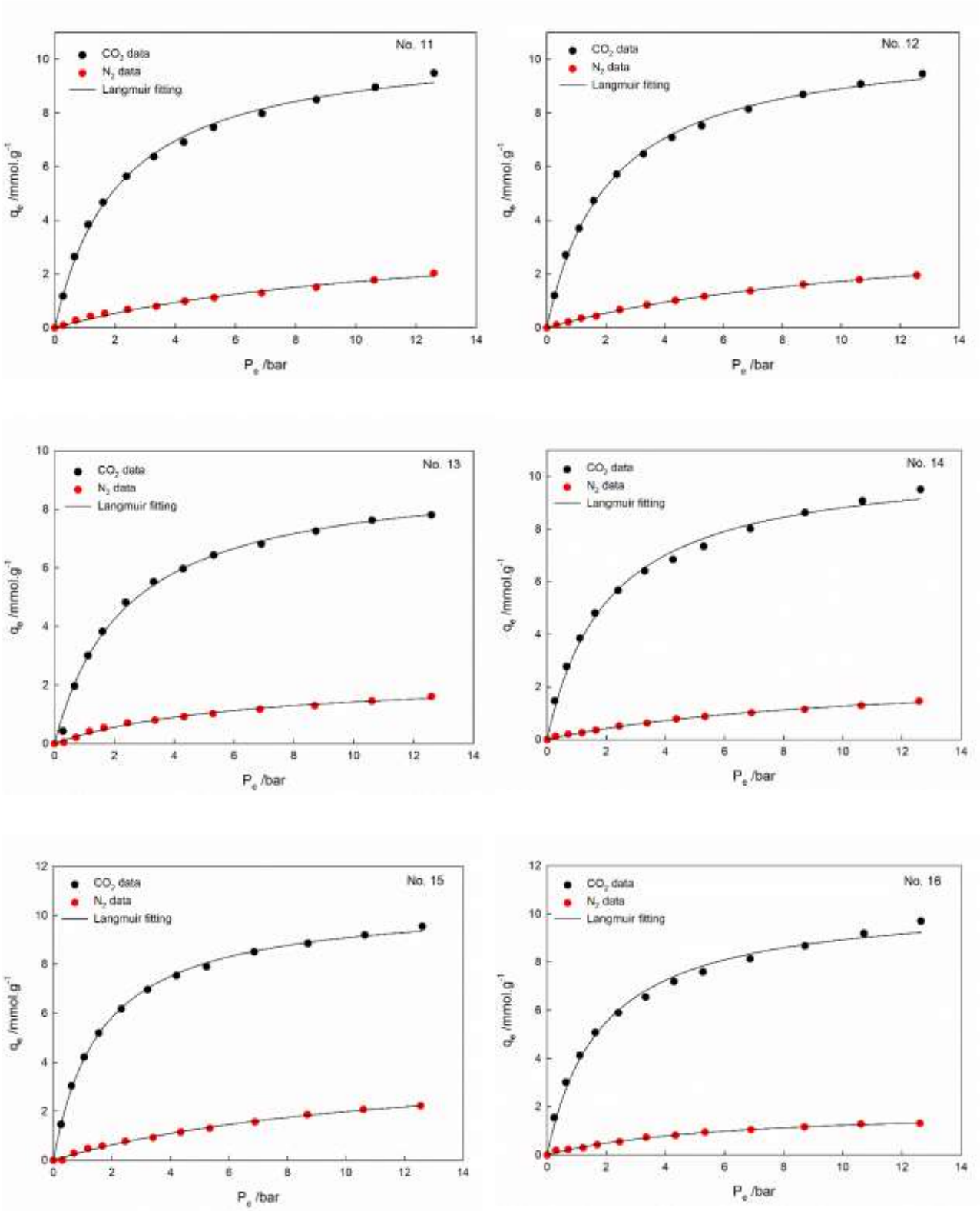

Fig. S1: CO_2 and N_2 adsorption capacity of 16 synthesized $Cu_3(BTC)_2$ with their Langmuir fitting at 298 K

Then, the obtained Langmuir constants were used in IAST method to estimate the CO_2/N_2 selectivity of each sample. After determination of optimum condition for synthesis of $Cu_3(BTC)_2$, the adsorption capacity of optimum sample was evaluated for both CO_2 and N_2 gases. In this case, Langmuir and Freundlich isotherm models were applied to relate the adsorbed amount of CO_2 and N_2 at equilibrium pressure. The model equations with their constants are listed in Table S1.

Table S1: Model isotherm equations and their parameters

Model	**Equation**	**Parameters**
Langmuir	$q_e = \frac{q_{\max} K_L C_e}{(1+K_L C_e)}$	K_L /L.mg^{-1}, q_{max}/mg.g^{-1}
Freundlich	$q_e = K_F C_e^{\frac{1}{n}}$	K_F /mg g^{-1} (L.mg^{-1})$^{-1/n}$, n

The adsorption behavior of CO_2 and N_2 at three different temperatures (298, 308, 318 K) was studied and results are depicted in Fig. S2. The isotherm constants which were calculated through non-linear fit of equilibrium data are tabulated in Table S2.

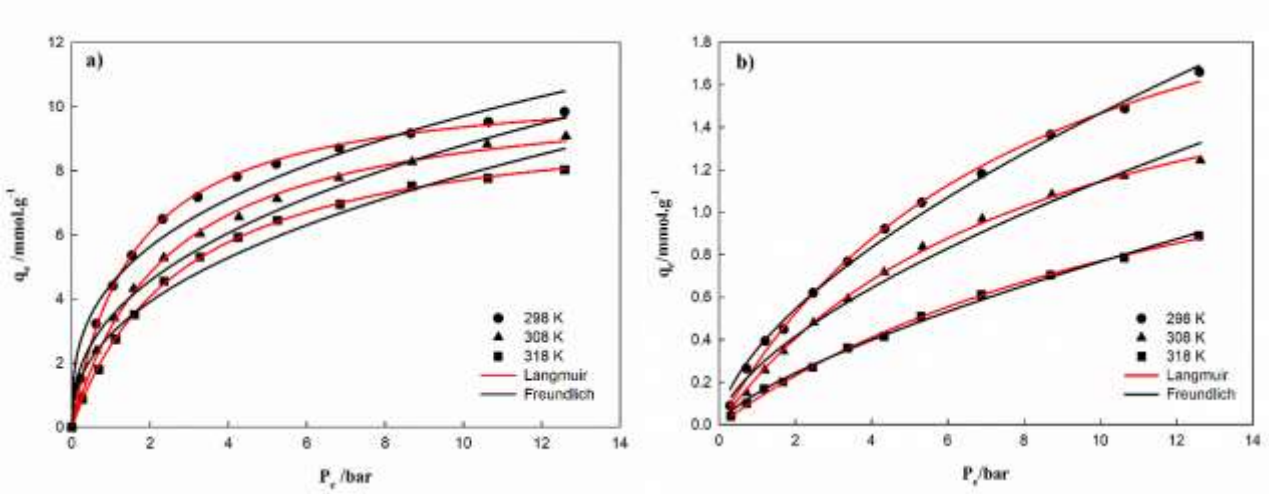

Fig. S2: Adsorption isotherms of a) CO_2 and b) N_2 on Opt-$Cu_3(BTC)_2$ at three different temperatures

Table S2: Langmuir and Freundlich isotherm constants for CO_2 and N_2 adsorption on Opt-$Cu_3(BTC)_2$

	CO_2			N_2		
Temperature /K	298	308	318	298	308	318
Langmuir						
q_m /mmol.g^{-1}	10.814	10.634	9.915	2.665	2.098	1.850
K_L /bar^{-1}	0.645	0.414	0.348	0.122	0.119	0.071
R^2	0.998	0.998	0.999	0.997	0.998	0.998
Freundlich						
K_F /mg g^{-1}(L.mg^{-1})$^{-1/n}$	4.457	3.445	2.901	0.354	0.267	0.147
n	2.960	2.456	2.308	1.622	1.585	1.397
R^2	0.970	0.977	0.971	0.994	0.982	0.996

With respect to correlation coefficients, Langmuir isotherm model interpreted the equilibrium data better than the Freundlich model which indicates that the adsorption-desorption process happens at the same rate per unit surface area of the microporous adsorbent [4]. It is visible that the adsorbed amount of CO_2 at 1 bar and 25 ℃, was 4.40 mmol.g^{-1} which is higher than the values reported in previous studies [5-8]. To explain the higher affinity of CuBTC for carbon dioxide, it should be noted that in general, there are two primary adsorption sites in the structure of $Cu_3(BTC)_2$. First one, is the unsaturated open Cu site, while the other is what it is known as "the small cage window site", where the CO_2 places in the four triangular-shaped openings into the small octahedral cage. Interestingly, each open Cu site can only accommodate one CO_2 molecule and the molecule may orient in four possible directions, with one end O atom attached to Cu atom. As expected, at low pressure, most CO_2 molecules go to the open metal sites. Only at

high loading is there a significant amount of CO_2 found on the small cage window site, as well as a small amount at two secondary adsorption sites (i.e., the center of the small octahedral cage and the corner of the large cuboctahedral cage, named small cage center site and large cage corner site, respectively) [9]. According to above-mentioned structural information of $Cu_3(BTC)_2$, CO_2 adsorption on this MOF can be explained as follow:

Except open metal sites, the framework- CO_2 interaction is mainly of van der Waals (vdW) type (which is also known "dispersion forces"), though the binding strength could vary depending on the shape of the local vdW surface. For CO_2 adsorption on the open metal sites, the binding is clearly stronger than a typical vdW interaction, as evidenced by the fact that, at low pressures, CO_2 is almost exclusively populated on the open metal sites. The enhanced overall binding presumably causes by the strong electrostatic interaction between the open metal ion and the CO_2 quadrupole moment. To better understand how open metal sites influence adsorption, Wu et. al [9] performed first-principles calculations based on density functional theory (DFT). Their inspection on electron density and projected charges showed that the charge distribution of the adsorbed CO_2 is also slightly redistributed. Since the metal-CO_2 interactions enhanced, it may cause the CO_2 molecule to be slightly polarized or even bent. Indeed, the calculated O-C-O bond angles from local density approximation (LDA) and general gradient approximation (GGA) were 178.7 and 179.4^0 for the CO_2 on open Cu. These observations suggested that upon adsorption on the open metal site, multipole moments are induced to the CO_2 molecule, which would lead to effective interaction between the open metal site and CO_2 molecule and consequently, enhanced overall binding. This issue was also approved by Dickey et. al [10] in which they investigated the influence of open metal sites on CO_2 adsorption through DFT method. They found that CO_2 molecules, cluster around the open metal sites; while, N_2 molecules were much less localised

than the CO_2 molecules. Since the CO_2 quadrupole moment is more than three times larger than the N_2 quadrupole moment (CO_2: 13.4? 0^{-40} C.m^2, N_2: 4.7×10^{-40} C.m^2), the CO_2 molecules creates stronger interactions with the electrostatic field of framework. To have better perception about the interaction on adsorption sites, Wu et. al conducted vibrational mode analysis of adsorbed CO_2. Based on first-principles calculations, they figured out that the adsorbed CO_2 molecule is affixed to the metal sites in an end-on orientation in which the closest oxygen is fixed while the rest of the molecule is quite “loose” (i.e., orientationally free) [9, 11]. This issue was also confirmed by Dietzel et. al. [12] in which they showed that at low pressures, CO_2 molecules coordinate with metal ion in the MOF structure and forms M^{2+}---O=C=O adducts with an end-on configuration. The oxygen lone pair orbitals of CO_2 interact with the copper cations, and in fact, the distance measured between the oxygen atom of CO_2 and the copper atom became shorter than the sum of their van der Waals radii.

It is a fact that adsorption temperature plays a crucial role in adsorption process and significantly affects the adsorption uptake. It is obvious from Fig.S2 that lower temperatures were more favorable for higher gas adsorption which indicates the exothermic nature of the process. This phenomenon can be expressed by the Boltzman equation in which the kinetic energy of gas molecules and the adsorbent at elevated temperatures is higher. This increase in kinetic energy would result in more interaction between gas molecules and adsorbent at the interface which leads to decrease in effective area of the sorbent that could be available for adsorption [8].

3. Effect of controlling factors and noise factor on $Cu_3(BTC)_2$ synthesis

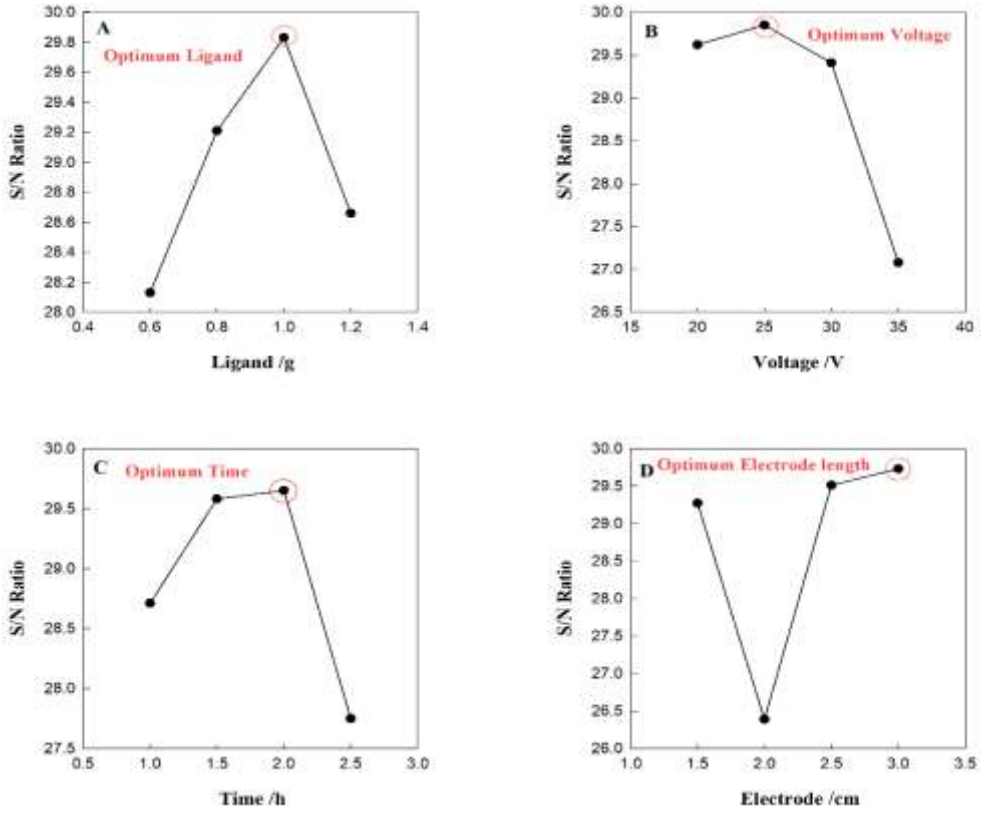

Fig. S3: The effect of controlling factors on selectivity

As can be seen from Fig. S3, increasing the electrode length from 2 to 3 cm, the S/N ratio and subsequently the selectivity were enhanced. This can be attributed to the fact that when the electrode surface area increases, more vacant sites will be available for nucleation and crystal formation. Furthermore, the concentration of copper ions increases in the extended area and makes this area more susceptible for new nucleation phenomenon and growth of adjacent crystals [13]. It is worth noting that, using longer electrode will provide a better condition for MOF islands to be distributed on the surface of the electrode and prevents the formation of compact layers of MOFs which may lead to decrease in porosity of MOFs [13]. Since the optimum point of electrode length was located at the end of the range, studying higher value

seemed to be imperative. In this regard, higher electrode length was checked and surprisingly, an odd occurrence in electrochemical cell was observed where black solids were dispersing in the synthesis solution. By further analysis it was found that, the black solids were copper oxide which were formed due to the high current density created between the electrodes. Higher current density causes more metal ions detach from electrode surface and disperse in the solution. Since excess amount of metal ions presented in the solution, there were not enough ligand to coordinate with them; hence, metal cores reacted with low amount of soluble oxygen in the synthesis solution and formed copper oxide. Besides, an extra increase in solution temperature caused partial vaporization of ethanol which reduced the involved length of electrode in synthesis solution and consequently, this occurrence brought problem in studying the effect of controlling factors on crystals formation. At the end of the synthesis process, a mixture of $Cu_3(BTC)_2$ crystals and copper oxide could be observed which was not desirable in this study. Electrolysis time was the second important factor in the synthesis of MOF. It is shown from Fig.1 that the selectivity raised steeply with increasing the electrolysis time. This trend continued up to 2h and then it was suddenly reduced. Generally, the increase of S/N ratio in the initial period of time, can be attributed to the formation of a thin layer of crystal on the surface of electrode under a constant voltage applied between the electrodes. After full-coverage of electrode with a crystal film, further MOF layer formation will happen in two regions: 1) MOF-substrate interface and 2) MOF-solution interface. In the latter condition, the solvated copper ions will pass through the MOF structure and reach to ligands to initiate nucleation, because the diameter of solvated copper ion (0.456nm) is smaller than pores of $Cu_3(BTC)_2$ (0.9nm). However, further reduction of S/N ratio and therefore the selectivity at higher synthesis time, may be due to compact layers of MOF film formed after 2h which inhibits or lowers copper ions transfer [13].

On the other hand, formation of these compact layers might create considerable resistance in solution followed by a drop in current rate which affects the formation and the quality of crystals. In studying the effect of voltage, it can be understood that high voltages (>25V) has a negative effect on the selectivity. When the voltage is raised from 20 to 25V, more copper ions will dissolve in solution leading to a better crystal growth and MOF nucleation. However, increasing the applied voltage from 25 to 35V expedites the reaction (redox) rate that inhibits the nucleation process. This factor may lead to unfavorable characteristics of the formed MOF such as insufficient pore volume or specific surface area to store CO_2 or separate CO_2 selectively. Although the amount of ligand does not have a significant effect on the selectivity according to the F-value, the S/N ratio changed by varying the amount of ligand. An increase in the amount of ligand (from 0.6 to 1g), had positive effect on selectivity; while, an opposite trend was observed when it was increased to 1.2g. This phenomenon may be attributed to the fact that when more ligands exist in the medium, less amount of Cu^{2+} will be produced and consequently, the surface of the copper electrode will be covered with less amount of $Cu_3(BTC)_2$ [14]. This might be attributed to slow reacting species that is formed during the formation of $Cu_3(BTC)_2$. Due to the existence of high amount of BTC ligand in the solution, these species tend to form an intermediate slow-reacting compound and hence, do not take part in the formation of $Cu_3(BTC)_2$ on the surface of the electrode [14].

4. Development of regression model

Fig. S4 compares predicted selectivity data based on Eq. (4) in terms of experimental values. As can be seen from Fig. S4, the majority of data are distributed around the regression line fitted the data with R^2=0.936 which means that 93.6% of experimental data agreed well with predicted ones.

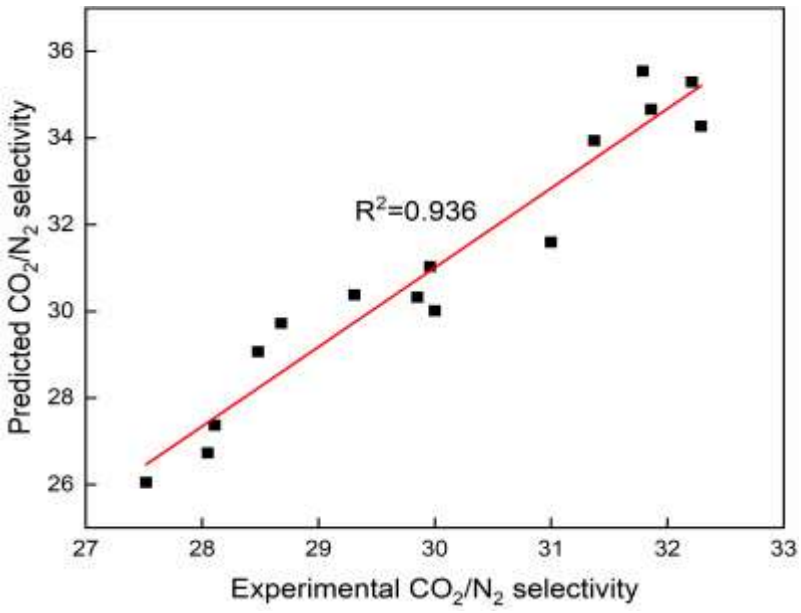

Fig. S4: Predicted versus actual CO_2/N_2 selectivity

5. Optimum ANN network architecture

Recognition of optimum network architecture comprises of finding an architecture with appropriate number of hidden layers and neurons as well as the transfer function available in each hidden layer. Table S3 summarizes the obtained results for RMSE and regression coefficients of some evaluated network architectures. As could be seen, in the architecture with one hidden layer, the number of neuron(s) was in the range of 1 to 20, whereas for the architecture with two hidden layers, the number of neuron(s) varied from 1 to 10 for each hidden layer. In addition, as could be seen, this table comprises of two distinct columns which is associated with networks utilizing “tansig” or “logsig” transfer function as logical component of their hidden layer(s). In addition, Table S4 summarizes weights and biases associated with each layer of optimum architecture.

Table S3: Network architecture and the errors associated with each architecture.

Network Architecture	"**tansig**" transfer function					"**logsig**" transfer function				
	RMSE	Regression Coefficient (r)				RMSE	Regression Coefficient (r)			
		Training	Validation	Testing	All Data		Training	Validation	Testing	All Data
1-1	27.704	0.746	0.566	0.622	0.673	26.656	0.619	0.740	0.823	0.680
5-1	25.393	0.722	0.787	0.674	0.712	21.368	0.921	0.593	0.565	0.828
10-1	9.179	0.999	0.588	0.995	0.968	6.707	0.999	0.995	0.899	0.983
15-1	19.505	0.958	0.940	0.512	0.906	17.208	0.997	0.753	0.891	0.904
20-1	19.143	1.000	0.931	0.939	0.968	20.784	0.961	0.517	0.658	0.854
1-1-1	34.490	0.929	0.838	0.940	0.892	27.467	0.704	0.684	0.598	0.665
5-1-1	9.713	0.990	0.944	0.955	0.968	5.048	0.995	0.979	0.994	0.991
10-1-1	6.399	0.999	0.950	0.982	0.996	11.813	0.992	0.965	0.820	0.953
5-2-1	11.837	0.993	0.968	0.887	0.988	13.113	0.999	0.939	0.826	0.935
10-2-1	25.390	0.976	0.990	0.936	0.958	11.510	0.973	0.959	0.953	0.967
5-3-1	31.306	0.904	0.997	0.690	0.913	13.358	0.995	0.958	0.881	0.946
10-3-1	9.356	0.999	0.989	0.829	0.968	7.695	0.993	0.959	0.969	0.978
5-4-1	7.144	0.988	0.979	0.965	0.980	4.552	0.999	0.982	0.953	0.992
10-4-1	6.760	1.000	0.998	0.837	0.996	4.308	0.999	0.962	0.956	0.993
5-5-1	15.724	0.981	0.966	0.914	0.979	11.347	0.966	0.904	0.897	0.952
7-5-1	**9.069**	**0.975**	**0.985**	**0.952**	**0.974**	**1.911**	**1.000**	**0.995**	**0.997**	**0.999**
10-5-1	8.154	0.977	0.997	0.924	0.974	5.638	0.997	0.992	0.972	0.989
5-6-1	5.706	0.999	0.984	0.952	0.988	4.293	0.996	0.998	0.951	0.993
10-6-1	5.662	0.989	0.989	0.970	0.987	5.819	0.992	0.967	0.985	0.988
5-7-1	13.327	0.970	0.909	0.950	0.933	7.596	0.999	0.988	0.829	0.977
10-7-1	5.850	0.999	0.968	0.988	0.987	9.337	0.987	0.979	0.987	0.973
5-8-1	15.548	0.999	0.990	0.937	0.947	13.571	0.999	0.984	0.886	0.944
10-8-1	7.328	0.999	0.995	0.974	0.984	4.748	0.999	0.952	0.976	0.991
5-9-1	7.210	1.000	0.997	0.833	0.980	5.384	0.998	0.997	0.821	0.989
10-9-1	8.495	0.992	0.986	0.928	0.975	4.891	0.991	0.991	0.954	0.990
5-10-1	7.534	0.993	0.990	0.905	0.979	4.717	0.994	0.990	0.989	0.991
10-10-1	10.526	0.999	0.966	0.931	0.967	6.998	0.998	0.951	0.543	0.981

Table S4: Weights and Biases for each layer of optimum architecture.

	Weights								Biases							
	Neuron	**1**	**2**	**3**	**4**	**5**	**6**	**7**		**1**	**2**	**3**	**4**	**5**	**6**	**7**
First Hidden Layer	W_{ij}	-2.878	3.265	3.088	-3.901	-6.350	-2.737	-2.115	b_j	0.130	0.311	-10.523	0.375	-2.542	-1.125	-4.834
		5.450	-8.848	1.860	-6.494	-3.699	-7.180	-1.855								
		-0.352	-3.584	6.413	-3.890	4.554	9.365	4.671								
		-2.006	2.356	-3.574	7.486	-1.852	1.845	0.015								
		1.055	15.941	0.921	4.206	-3.961	-0.598	0.829								
		-1.557	-0.629	-10.871	-0.491	1.924	1.070	0.928								
		-2.878	3.265	3.088	-3.901	-6.350	-2.737	-2.115								
Second Hidden Layer	W_{jk}	6.248	-5.922	-0.884	2.244	-0.238			b_k	-10.058	-0.886	3.538	3.752	-6.075		
		3.943	1.199	-2.950	1.081	1.417										
		3.067	10.900	5.733	0.192	-1.996										
		1.780	10.119	-2.425	8.003	1.643										
		-0.469	1.180	-4.829	0.624	3.377										
		1.453	3.982	8.176	4.312	4.191										
		3.238	2.989	4.875	3.729	-3.120										
Output Layer	W_{kl}	-0.893							b_l	-2.648						
		2.123														
		2.467														
		-0.595														
		1.099														

References

[1] Mishra P, Mekala S, Dreisbach F, Mandal B, Gumma S, Adsorption of CO2, CO, CH4 and N2 on a zinc based metal organic framework. Separation and Purification Technology, 2012, 94: 124-130.

[2] Krishna R, Adsorptive separation of CO2/CH4/CO gas mixtures at high pressures. Microporous and Mesoporous Materials, 2012, 156: 217-223.

[3] Chowdhury S, Balasubramanian R, Highly efficient, rapid and selective CO 2 capture by thermally treated graphene nanosheets. Journal of CO2 Utilization, 2016, 13: 50-60.

[4] Sarker A I, Aroonwilas A, Veawab A, Equilibrium and Kinetic Behaviour of CO2 Adsorption onto Zeolites, Carbon Molecular Sieve and Activated Carbons. Energy Procedia, 2017, 114: 2450-2459.

[5] Zhou X, Huang W, Miao J, Xia Q, Zhang Z, Wang H, Li Z, Enhanced separation performance of a novel composite material GrO@ MIL-101 for CO2/CH4 binary mixture. Chemical Engineering Journal, 2015, 266: 339-344.

[6] Zhou Z, Mei L, Ma C, Xu F, Xiao J, Xia Q, Li Z, A novel bimetallic MIL-101 (Cr, Mg) with high CO2 adsorption capacity and CO2/N2 selectivity. Chemical Engineering Science, 2016, 147: 109-117.

[7] Armstrong M R, Shan B, Cheng Z, Wang D, Liu J, Mu B, Adsorption and diffusion of carbon dioxide on the metal-organic framework CuBTB. Chemical Engineering Science, 2017, 167: 10-17.

[8] Salehi S, Anbia M, High CO2 adsorption capacity and CO2/CH4 selectivity by nanocomposites of MOF-199. Energy & Fuels, 2017, 31 (5): 5376-5384.

[9] Wu H, Simmons J M, Srinivas G, Zhou W, Yildirim T, Adsorption sites and binding nature of CO2 in prototypical metal− organic frameworks: A combined neutron diffraction and first-principles study. The Journal of Physical Chemistry Letters, 2010, 1 (13): 1946-1951.

[10] Dickey A N, Yazaydın A Ö, Willis R R, Snurr R Q, Screening CO2/N2 selectivity in metal-organic frameworks using Monte Carlo simulations and ideal adsorbed solution theory. The Canadian Journal of Chemical Engineering, 2012, 90 (4): 825-832.

[11] Bordiga S, Regli L, Bonino F, Groppo E, Lamberti C, Xiao B, Wheatley P, Morris R, Zecchina A, Adsorption properties of HKUST-1 toward hydrogen and other small molecules monitored by IR. Physical Chemistry Chemical Physics, 2007, 9 (21): 2676-2685.

[12] Dietzel P D, Johnsen R E, Fjellvåg H, Bordiga S, Groppo E, Chavan S, Blom R, Adsorption properties and structure of CO 2 adsorbed on open coordination sites of metal–organic framework Ni 2 (dhtp) from gas adsorption, IR spectroscopy and X-ray diffraction. Chemical Communications, 2008, (41): 5125-5127.

[13] Campagnol N, Van Assche T R, Li M, Stappers L, Dincă M, Denayer J F, Binnemans K, De Vos D E, Fransaer J, On the electrochemical deposition of metal–organic frameworks. Journal of Materials Chemistry A, 2016, 4 (10): 3914-3925.

[14] Schäfer P, *Electrochemical growth of CuBTC: improving the synthesis toolkit through mechanistic understanding*. Dissertation, Mainz, Johannes Gutenberg-Universität, 2017.